Materials Today • Volume xxx, Number xx • xxxx 2021 RESEARCH

ELSEVIER

RESEARCH: Original Research

A hierarchical $Ti_2Nb_{10}O_{29}$ composite electrode for high-power lithium-ion batteries and capacitors

Tao Yuan [1,2,†], Sainan Luo [1,†], Luke Soule [2], Jeng-Han Wang [3], Yachen Wang [3], Dewang Sun [1], Bote Zhao [2], Wenwu Li [2], Junhe Yang [1], Shiyou Zheng [1,*], Meilin Liu [2,*]

[1] School of Materials Science and Engineering, University of Shanghai for Science and Technology, Shanghai 200093, China
[2] School of Materials Science and Engineering, Georgia Institute of Technology, Atlanta, GA 30332-0245, United States
[3] Department of Chemistry, National Taiwan Normal University, 88, Sec. 4 Ting-Zhou Road, Taipei 11677, Taiwan, ROC

$Ti_2Nb_{10}O_{29}$ (TNO) is a suitable electrode for high-performance lithium-ion batteries and capacitors because of its large lithium storage capacity and high Li^+ diffusivity. Currently, the rate or power capability of TNO-based systems is limited by the poor electronic conductivity of the material. Here we report our findings in design, synthesis, and characterization of a hierarchical N-rich carbon conductive layer wrapped TNO structure (TNO@NC) using a novel polypyrrole-chemical vapor deposition (PPy-CVD) process. It was found that carbon coating with PPy–carbon partially reduces Ti and Nb cations, forms TiN, and creates oxygen vacancies in the TNO@NC structure that further increase overall electronic and ionic conductivity. Various defect models and density functional theory (DFT) calculations are used to show how oxygen vacancies influence the electronic structure and Li-ion diffusion energy of the TNO@NC composite. The optimized TNO@NC sample shows notable rate capability in half-cells with a reversible capacity of 300 mAh g^{-1} at 1 C rate and maintains 211 mAh g^{-1} at a rate of 100 C, which is superior to that of most $M_xNb_yO_z$ materials. Full cell $LiNi_{0.5}Mn_{1.5}O_4$ (LNMO)||TNO@NC lithium-ion batteries (LIB) and active carbon (AC)||TNO@NC hybrid lithium-ion capacitors (LIC) exhibited notable volumetric and gravimetric energy and power densities.

Introduction

One of the primary barriers to wide-spread electric vehicle adoption is the slow charging speeds required to drive a reasonable distance (200 miles or more). The DOE outlines a fast charging goal of 15 min charge to 80% of pack capacity, which is out of reach for commercial battery technology today [1]. While hybrid technologies based on metal ion-capacitors show promise to achieve reasonable charge/discharge rates while maintaining suitable energy densities [2,3], further improvements in all aspects of battery design are needed to create fast-charging batteries. For fast-charging applications, $Ti_xNb_yO_z$ oxides, such as $TiNb_{24}O_{62}$ [4,5], $Ti_2Nb_{10}O_{29}$ [6,7], $TiNb_2O_6$ [8], and $TiNb_2O_7$ [9,10] are promising anode materials for long-life and high-rate LIBs and hybrid LICs systems. The crystal structure of $Ti_xNb_yO_z$ oxides are of the same structure family as H-Nb_2O_5, which can be described as a defective ReO_3-like structure where crystallographic shear planes cut the structure into blocks, typically 3–4 octahedra long in length and width [11]. While initial papers claimed that Ti^{4+} randomly substitutes for Nb^{5+} in octahedral [12], neutron scattering experiments have revealed that Ti^{4+} selectively occupies corner and edge sites of the blocks rather than randomly through the structure [13]. The nature of the fast ionic conductivity of the material as well as the lithiation mechanism of the oxide is an active topic of research, with some papers putting forth a reversible "single-phase ↔ two-phase ↔ single-phase" reaction pathway during the batteries

* Corresponding authors.
E-mail addresses: Zheng, S. (syzheng@usst.edu.cn), Liu, M. (meilin.liu@mse.gatech.edu).
† These authors contributed equally to this work.

 https://doi.org/10.1016/j.mattod.2020.11.018

Please cite this article in press as: T. Yuan et al., Materials Today (2021), https://doi.org/10.1016/j.mattod.2020.11.018

charge–discharge processes [5,14,15]. $Li_4Ti_5O_{12}$ (LTO) is currently regarded as the state-of-the-art high power LIBs anode [16–18], and $Ti_xNb_yO_z$ compounds can store substantially more lithium ions at low and high rates than this compound [19]. Additionally, compared with very flat voltage plateau of LTO, $Ti_xNb_yO_z$ compounds typically display a predictable sloping behaviour at the end of a charge/discharge cycle, making the prediction of cycle termination straightforward [20,21].

Even though $Ti_xNb_yO_z$ compounds show notable rate-capability, they are limited by their low electronic conductivity ($<10^{-9}$ S cm^{-1}), which is attributed to empty 3d/4d orbitals in the Ti/Nb metal d-band [22,23]. To overcome the poor electrical conductivity of the material, two strategies have been widely used, including carbon coating [22,24], and nanostructuring [25,26]. While these strategies have greatly enhanced the rate performance of $Ti_xNb_yO_z$ composite electrodes, there are sacrifices that must be made. Due to the inherently low density of carbon, techniques that use the material to compensate for poor electronic conductivity of active materials will decrease the packing efficiency of the electrode material and result in inherently low volumetric capacities [27]. This is in addition to the 10–20 % carbon that is already used to make typical battery electrodes [28–30]. For nanostructured material, such as nanofibers, nanotubes, and three dimensional aerogels, geometric constraints and high surface energies prevent efficient packing of active material and further decrease the overall volumetric capacity of the electrode [31]. In addition to these issues, processing of nanomaterials is often costly, needs to utilize non-aqueous medium and special equipment, and is usually difficult to scale to industrial levels [32]. Solid state synthesis is common used for large-scale production of phase-pure $Ti_xNb_yO_z$ oxides with oxide precursors and firing temperature up to 1000 °C [20,33,34]. At these calcination temperatures, the synthesized powder has particle sizes that vary between 20 and 50 μm [20,33,34]. While solid state synthesis is a clear route to achieve efficient packing of active material, the problem of insufficient electronic conductivity still needs to be addressed.

To this end, we utilized ball-milling and a PPy–CVD solid-state synthesis method to coat $Ti_2Nb_{10}O_{29}$ (TNO) nanoparticles with a thin layer of nitrogen-doped PPy–carbon that does not significantly decrease the tap-density of the material. The composite allows for sufficient electrical conductivity and acceptable volumetric capacity. The prepared TNO@NC architecture can be described by agglomerated secondary particles (200–800 nm) which are composed of smaller nanoparticles (~40 nm). This architecture allows for short Li^+ diffusion paths between nanoparticles and a high packing density afforded by large secondary particles. In addition to highly conductive N-doped carbon thin-films coated on the particles, XPS shows that Ti^{4+} and Nb^{5+} ions are partially reduced and that conductive Ti–N is formed *in situ* during the carbonthermal calcination process. EPR results further confirm the existence of oxygen vacancies in the TNO@NC structure, and DFT calculations demonstrate that oxygen vacancies improve both the electronic and ionic conductivities of the TNO@NC materials. The hierarchical structure of the electrode allows for fast lithium insertion/extraction kinetics as well as considerable packing density, resulting in the fabrication of a full cell LIB and LIC that shows promising gravimetric and volumetric power and energy density.

Experimental section

Fabrication of the TNO@NC composite

The TNO@NC composite was synthesized by a PPy-CVD assisted solid-state reaction process. Briefly, 5 g of Nb_2O_5 powder (Aladdin Reagent Co. Ltd., AR, 99.9%) was ball milled in DI water using a Pulverisette-6 planetary mill with 80 ml grinding bowls (Fritsch Co.) at a rotational speed of 500 rpm for 4 h. After ball milling, the dried material was dispersed in 10 g of 20 wt.% Fe (III) p-toluenesulfonate (Sigma-Aldrich) n-butanol solution to cover the surface of the Nb_2O_5 particles with Fe^{3+} ions, which act to polymerize the pyrrole monomer to polypyrrole on the surface of particles [35]. Then, the mixture was transferred into a sealed container with 1 ml of pyrrole that released pyrrole monomer vapor at room temperature, which interacted with the Fe^{3+} ions on the surface of the particles to polymerize to polypyrrole. After 45 min, the powder was taken out of the container and centrifuged with ethanol several times to remove any $Fe^{3+/2+}$ salts and residual pyrrole monomers. The sample at this stage will be denoted as Nb_2O_5@PPy. Nb_2O_5@PPy was hand-ground with a stoichiometric amount of metatitanic acid [$TiO(OH)_2$] (Jinjinle Chemical Co. Ltd., CP, 99 %) for 1 h. The resulting powder was calcined at various temperatures between 600 and 1000 °C for 20 h under a nitrogen atmosphere. As a control sample, $Ti_2Nb_{10}O_{29}$ was prepared via solid-state reaction with Nb_2O_5 powder and anatase TiO_2 (Aladdin Reagent Co. Ltd., 99.8%, primary particle size: 30 nm) as the niobium and titanium source, respectively. The initial reagents were hand-ground for 1 h and fired in air between 800 and 1100 °C for 20 h.

Material characterization

The morphology of the synthesized material was observed using an ultrahigh-resolution field-emission scanning electron microscope (FE-SEM) (INCA X-Max 80, Oxford Instruments) and a transmission electron microscope (TEM) (JEM-2100F, JEOL, Ltd., Japan). X-ray diffraction (XRD) patterns were recorded on a Rigaku D/MAX-2200/PC X-ray diffractometer at 40 kV and 20 mA, with a Cu Ka radiation in the 2-theta range from 10 to 70°. The amount of carbon contributed by the PPy layer in the Nb_2O_5@PPy and TNO@NC composite was determined by thermogravimetric analysis (TGA) using a Netzsch STA 449 F1 with a heating rate of 10 °C min^{-1} in air atmosphere. Porosity and Brunauer–Emmett–Teller (BET) surface areas for the samples were measured using a nitrogen sorption instrument (Micromeritics, ASAP2020). The surface elements and corresponding valence states of the samples were analyzed using an XPS (Kratos Axis Ultra DLD). EPR spectra of the pristine TNO and TNO@NC samples were acquired using an EPR spectrometer (Bruker A320) at room temperature. The tap densities were measured according to the ASTM international standard B527-15, modified to accommodate a 5–10 cm^3 graduated cylinder with the rate of ~200 taps per minute. The electrical conductivity of the obtained TNO@NC material was measured by a four-point probe method (RTS-9) at room temperature. The samples for the electrical conductivity measurement were prepared by pressing the TNO@NC powders

Please cite this article in press as: T. Yuan et al., Materials Today (2021), https://doi.org/10.1016/j.mattod.2020.11.018

into a pellet (10 mm in diameter and 1 mm in thickness) under a pressure of 20 MPa.

Electrode fabrication

For half-cell tests of the TNO@NC and control TNO anodes, 2032-type coin cells were used. The active electrodes were prepared using a slurry containing 85 wt % active material, 8 wt % carbon black, and 7 wt % polyvinylidene fluoride (PVDF) in N-methyl-2-pyrrolidone (NMP). The slurry was coated on a copper foil current collector. The mass loading of active material was approximately 1.4 mg cm^{-2}, and the electrochemical performances using higher mass loading of 3.3 and 6.7 mg cm^{-2} have also been studied. The electrodes were punched to a diameter of 1.2 cm and then dried in a vacuum oven at 100 °C for 24 h before being transferred to the glovebox. The coin cells were assembled in the glovebox with lithium metal as the counter and reference electrodes, a microporous polypropylene Celgard 3501 (Celgard, LLC Corp., USA) as a separator, and 1 M LiPF6/EC/DMC (1:1 by volume ratio) as the electrolyte.

For the full cell tests, the commercial $LiNi_{0.5}Mn_{1.5}O_4$ (MJS Energy Technology Co., Ltd) and active carbon (AC) (Kuraray Co., Ltd.) were used as the cathode materials for LIB and LIC, respectively. The $LiNi_{0.5}Mn_{1.5}O_4$ cathode was prepared using a slurry containing 80 wt% $LiNi_{0.5}Mn_{1.5}O_4$ active material, 10 wt % carbon black, and 10 wt% PVDF in NMP. The active carbon cathode (AC) was prepared using a slurry containing AC, carbon black and carboxymethyl cellulose (CMC) at the weight ratio of 80:10:10 in water. The weight ratios of cathodes to anodes in the LIB and LIC full cells were carefully balanced based on the specific capacity of $LiNi_{0.5}Mn_{1.5}O_4$ or AC cathodes and TNO@NC anode. The weight ratio of cathode to anode for the LNMO||TNO@NC LIB is 2.1 and for the AC||TNO@NC LIC is 6.6, respectively. The current densities and corresponding specific capacities are calculated based on the mass of the anodic active material.

Computational method

All the computational works were performed by Vienna Ab Initio Simulation Package (VASP) [36–39]. The computational level was at the GGA-PW91 level that the exchange–correlation function was treated by generalized gradient approximation with Perdew-Wang 1991 formula [40,41]. The core electrons were treated with cost-effective pseudopotentials implemented in VASP and the valence electron were expanded by plane-wave basis set with the kinetic cutoff (maximum) energy at 600 eV, the projector-augmented wave (PAW) method [42,43]. The integrations in the reciprocal space at Brillouin-Zone (BZ) were sampled by Monkhorst-pack scheme at 0.05 × 2 (1/Å) interval [44]. The quasi-Newton method with the energetic and gradient convergences at 1×10^{-4} and 1×10^{-2} eV, respectively, was employed for the structural optimization and energetic calculations.

The pure TNO anode was modeled by the double-sized supercell containing 4 Ti, 20 Nb and 58 O atoms. The TNO@NC with oxygen vacancy ($Ti_4Nb_{20}O_{58-x}$) was modeled by removing O atoms (according to × values) from pure TNO; the locations of removed O atoms in the Ti and Nb pairs are both considered to examine the preferential defect sites in TNO. The modeled structures were optimized and the related energies were utilized for the defect (oxygen vacancy) formation energy calculation. The density of states (DOS) of the Ti d-band, Nb d-band, O p-bands of the pure and defective TNO were further analyzed to examine the change of electronic conductivity upon defect formation.

Results and discussion

Fig. 1 schematically illustrates the preparation of the TNO@NC composite and corresponding TEM images during each stage of the process. As shown in Fig. 1b and c, the particle-size of the Nb_2O_5 starting material was reduced from micron-sized bulk material to ~30 nm after high-energy ball milling (HEBM). The particles were then carbon coated using a modified PPy-CVD method. After HEBM, the nano-Nb_2O_5 particles were thoroughly dispersed in a Fe(III) tosylate solution in order to cover the material with a layer of oxidant. The Fe(III) coating layer acts as an initiator of the chemical polymerization of pyrrole. To deposit the polypyrrole film, Nb_2O_5@Fe^{3+} was placed into a container filled with pyrrole vapor. Pyrrole molecules deposit on the surface of the particles and polymerize to form polypyrrole, denoted as PPy. Simultaneously, Nb_2O_5 nanoparticles agglomerate into lar-

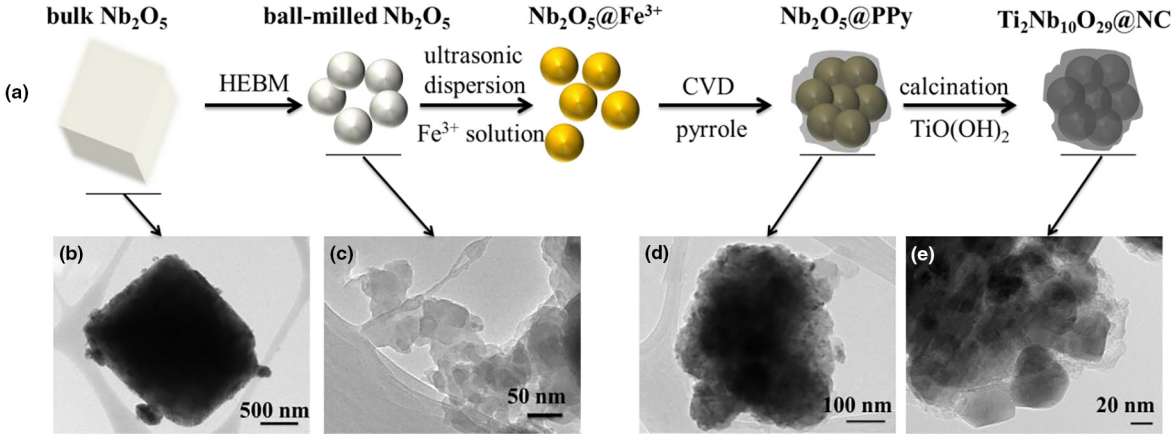

FIGURE 1

Illustration of the synthetic route for TNO@NC composites (a); and the corresponding TEM images of (b) bulk Nb_2O_5 raw material, (c) ball milled Nb_2O_5, (d) PPy coated Nb_2O_5 and (e) TNO@NC.

Please cite this article in press as: T. Yuan et al., Materials Today (2021), https://doi.org/10.1016/j.mattod.2020.11.018

ger particles on the order of 200–300 nm (Fig. 1d). The larger secondary particle size is beneficial to increase the tap density of the material so as to increase the volumetric energy and power density of the battery [31]. The PPy coating also seems to inhibit the sintering of the TNO particles at 800 °C as seen in the particle size difference between TNO@NC (Fig. 1e) and pristine TNO (Fig. S1).

The phase of the synthesized TNO@NC products at various calcination temperatures ranging from 600 to 1000 °C for 20 h was confirmed by XRD and is shown in Fig. S2. When the calcination temperature was 600 °C, the phase of the product appears to be a bronze structure similar to T-Nb_2O_5 [11]. When the calcination temperature is increased to 700 °C, the monoclinic-TNO phase appears and consumes the bronze phase. As the calcination temperature reaches 800 °C, the bronze phase is primarily gone, with only two faint peaks present at 22.7° and 28.3°. The diffraction peaks are consistent with the crystal planes of $Ti_2Nb_{10}O_{29}$ (JCPDS 72–0159), which indicate that the obtained sample is pure monoclinic TNO [33,45]. This calcination temperature, 800 °C, is 100 °C lower than required in a solid-state reaction using anatase-TiO_2 as a titanium precursor (Fig. S3) [20,33]. This phenomenon can be understood by the lower cohesive energy of the Ti-OH bond (284 kJ mol^{-1}) in the metatitanic acid molecule precursor [$TiO(OH)_2$] as compared to the O=Ti=O bond (873.6 kJ mol^{-1}) in anatase TiO_2 [46]. The monoclinic phase of TNO is also obtained at higher calcination temperature of 900 °C and 1000 °C, with the peak intensity higher than that of the 800 °C sample, suggesting the improved crystallinity of the oxide with temperature. The morphologies of the particles are shown in Fig. S4. It can be seen that the secondary particle size of the sample calcined at 800 °C is similar to those of the ones calcined at 600 °C and 700 °C, due likely to the effect of the carbon layer on particle growth. The particle size of the sample calcined at 900 °C is slightly larger than that of the sample calcined at 800 °C (400–500 nm). The particle size increased to ~1 μm after calcination at 1000 °C for 20 h, indicating that the effect of carbon layer on particle growth disappeared at higher temperatures. The thickness and morphology of the carbon layer were investigated using TEM.

Fig. 2 shows the TEM images and the corresponding elemental distribution of the TNO@NC composite. As shown in Fig. 2a, the material shows particle sizes around 40 nm and is encapsulated by a continuous carbon layer with a thickness of ~ 1–4 nm (Fig. 2b). The carbon content in the composite was ~ 1.8 wt.% by TGA analysis (Fig. S5). Two d-spacing values of 0.35 and 0.28 nm were measured in HRTEM lattice image in Fig. 2b, which are in good agreement with the d-spacing of the (400) and ($21\bar{5}$) planes for monoclinic TNO, respectively. The EDS result in Fig. 2c verifies the homogenous coating of the particles by PPy derived carbon, and that the film contains a large amount of nitrogen. Some have proposed in literatures that N-doping alters the surface electron density of oxide materials and in-turn enhances the ion and electron transfer kinetics [47,48].

XPS was used to quantify the amount of N in the TNO@NC sample and to probe the valence state of each cation in the pristine TNO and TNO@NC samples (Fig. S6). The ratios of each element are listed in Table S1. By fitting the high resolution XPS spectra of Ti2p and Nb3d (Fig. 3a, b), it is found that some of the Ti^{4+} and Nb^{5+} are reduced, respectively, to Ti^{3+} and Nb^{4+} in the TNO@NC composite [7,47,49,50]. As shown by the corresponding ratios of different valences of Ti2p and Nb3d listed in Table S2 and Table S3, considerable Ti^{3+} (50.7 at.% of Ti atoms) and Nb^{4+} (25.9 at.% of Nb atoms) are present on the surface of the TNO@NC sample. This amount of the reduced Ti^{3+} is greater than most reported values [49], due likely to *in situ* formation of Ti-N chemical bond [47], as confirmed by the N1s and C1s high resolution XPS spectra for the TNO@NC sample (Fig. S7) and the corresponding refinement results (Tables S4 and S5). Since the conductivity of TiN is relatively high, the electronic conductivity of TNO@NC composite is enhanced by the presence of TiN [51]. The electrical conductivity of TNO@NC (6.3×10^{-3} S cm^{-1}, as determined from four-point probe measurement) is about six

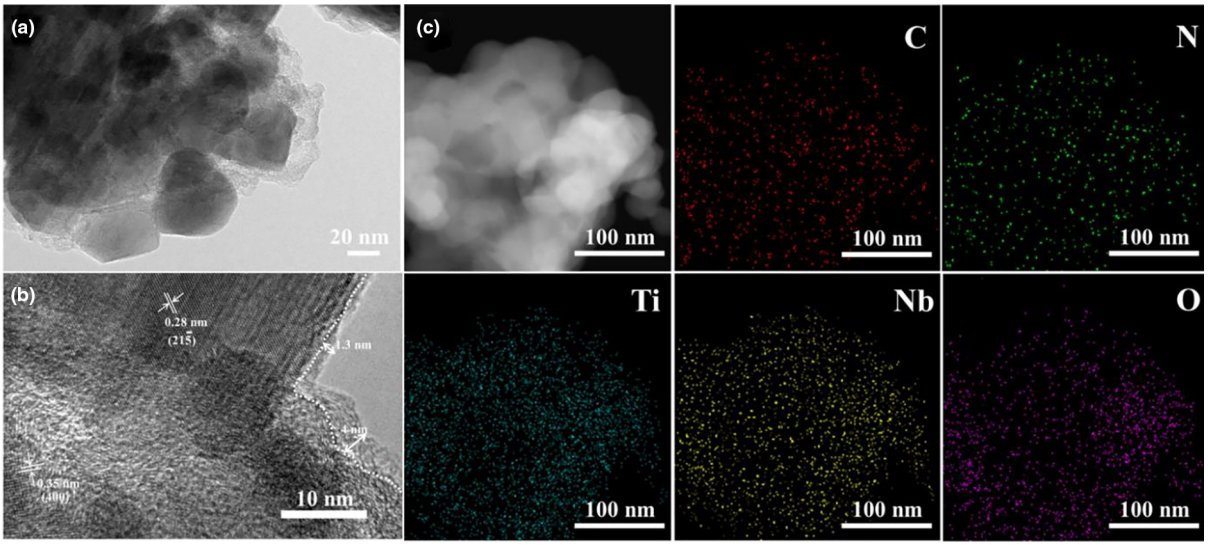

FIGURE 2

(a) TEM image (b) HRTEM image of TNO@NC composite and (c) the corresponding EDS mappings of C, N, Ti, Nb and O in the TNO@NC composite.

Please cite this article in press as: T. Yuan et al., Materials Today (2021), https://doi.org/10.1016/j.mattod.2020.11.018

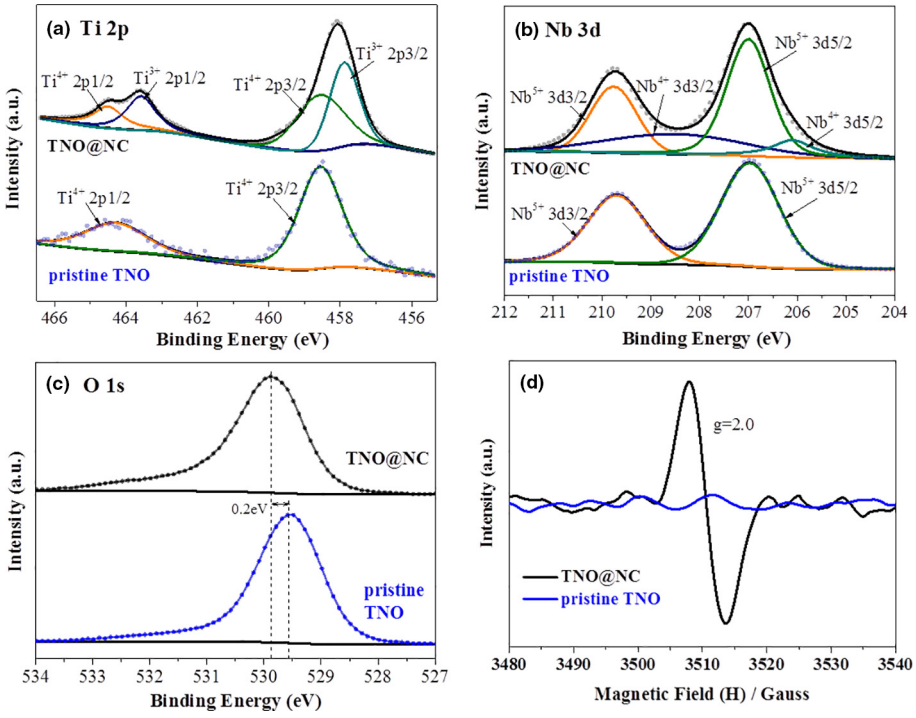

FIGURE 3

High-resolution XPS spectra of (a) Ti2p (b) Nb3d and (c) O1s of the pristine TNO and TNO@NC samples; (d) EPR spectra of the pristine TNO and TNO@NC samples.

orders of magnitude higher than that of the pure TNO (10^{-9} S cm^{-1}) [52]. The O 1 s spectra for the pristine TNO and TNO@NC samples are presented in Fig. 3c; the large peak at ~529.7 eV is shifted towards higher binding energy for the TNO@NC sample than the pristine TNO sample, implying some electron drain in the oxide matrix of the TNO@NC sample [53]. This means that some oxygen is missing from the lattice [54]. Also, as shown in the EPR spectra for the two samples (Fig. 3d), a strong EPR signal, indicative of the formation of oxygen vacancies at $g = 2.0$, is observed for the TNO@NC sample [55], but it is missing for the pure TNO sample, confirming the presence of oxygen deficiency in the TNO@NC sample.

It should be mentioned that modeling the defect structure of TNO@NC is difficult as the true amount of oxygen vacancies is uncertain. While XPS gives a rough estimate, the technique is surface sensitive and does not give information on the properties of the bulk material. To study the effect that defect formation on the electronic structure of TNO, we used DFT calculation to model TNO with a varied amount of oxygen vacancies. In the calculations, the TNO stoichiometry was doubled to $Ti_4Nb_{20}O_{58}$ and the oxygen vacancy concentration was varied from 1% to 12%, denoted as $Ti_4Nb_{20}O_{(58-x)}$ ($x = 0$, 1, 2, 3, 6 and 12) shown in Fig. S8. The calculation results are listed in Table S6 and the corresponding schematic structures are shown in Fig. 4a. It is noted that the average oxygen vacancy formation energies vary from 3.02 to 3.57 eV when the concentration of oxygen vacancies in the TNO structure ($Ti_4Nb_{20}O_{(58-x)}$, $x \leq 3$) is relatively small. Further, it is more energetically favorable for oxygen vacancy to form near Ti sites (3.02 eV) than Nb sites (3.50 eV), suggesting that it is easier to reduce Ti^{4+} than Nb^{5+}, which is consistent with the XPS results. As the population of oxygen vacancy increases, especially when more than 6 oxygen vacancies are present in the model unit of $Ti_4Nb_{20}O_{(58-x)}$ ($x = 6$ or 12), the average oxygen vacancy formation energy increases significantly (~5 eV) and the structure tends to be unstable. Accordingly, we further calculated the DOS and the Li-ion diffusion energy barriers for the $Ti_4Nb_{20}O_{(58-x)}$ ($x = 0$, 1, 2 and 3) models.

As shown in Fig. 4b, for the pristine TNO, more empty metal d bands (Ti or Nb) contribute to the conduction band (antibonding band) while highly occupied O p band contributes to the valence band (bonding band); this is the typical DOS for ionic metal oxides. In the presence of oxygen deficiency (Fig. 4c and Fig. S9), metal d bands become broader and shift to lower energies due mainly to the loss of the ionic characters in the absence of metal–oxygen bonds. The defect also lowers the energy of oxygen p band. As a result, the overall bandgap gradually decreases and the electronic conductivity improves as more oxygen deficiency is introduced in the TNO lattice. DFT calculation was used to examine the Li-ion diffusion pathways and the corresponding energy barriers in $Ti_4Nb_{20}O_{(58-x)}$ ($x = 0$, 1, 2 and 3), as shown in Fig. 4d. Both of the initial and final sites of Li-ion diffusion are the lowest energy sites. It could be seen that the diffusion energy barriers of the oxygen defective $Ti_4Nb_{20}O_{(58-x)}$ samples are lower than that of the pure $Ti_4Nb_{20}O_{58}$ sample. Additionally, Li-ion diffusion energy barriers decrease with the increase in oxygen deficiency in $Ti_4Nb_{20}O_{(58-x)}$, implying that oxygen deficiency in TNO facilitates Li-ion transport.

The electrochemical performance of TNO@NC was characterized under constant current charge–discharge cycling at 1 C rate between 1.0 and 3.0 V using a half cell consisting of a TNO@NC composite working electrode and a metallic lithium counter/reference electrode. As illustrated in Fig. 5a, the first discharge

Please cite this article in press as: T. Yuan et al., Materials Today (2021), https://doi.org/10.1016/j.mattod.2020.11.018

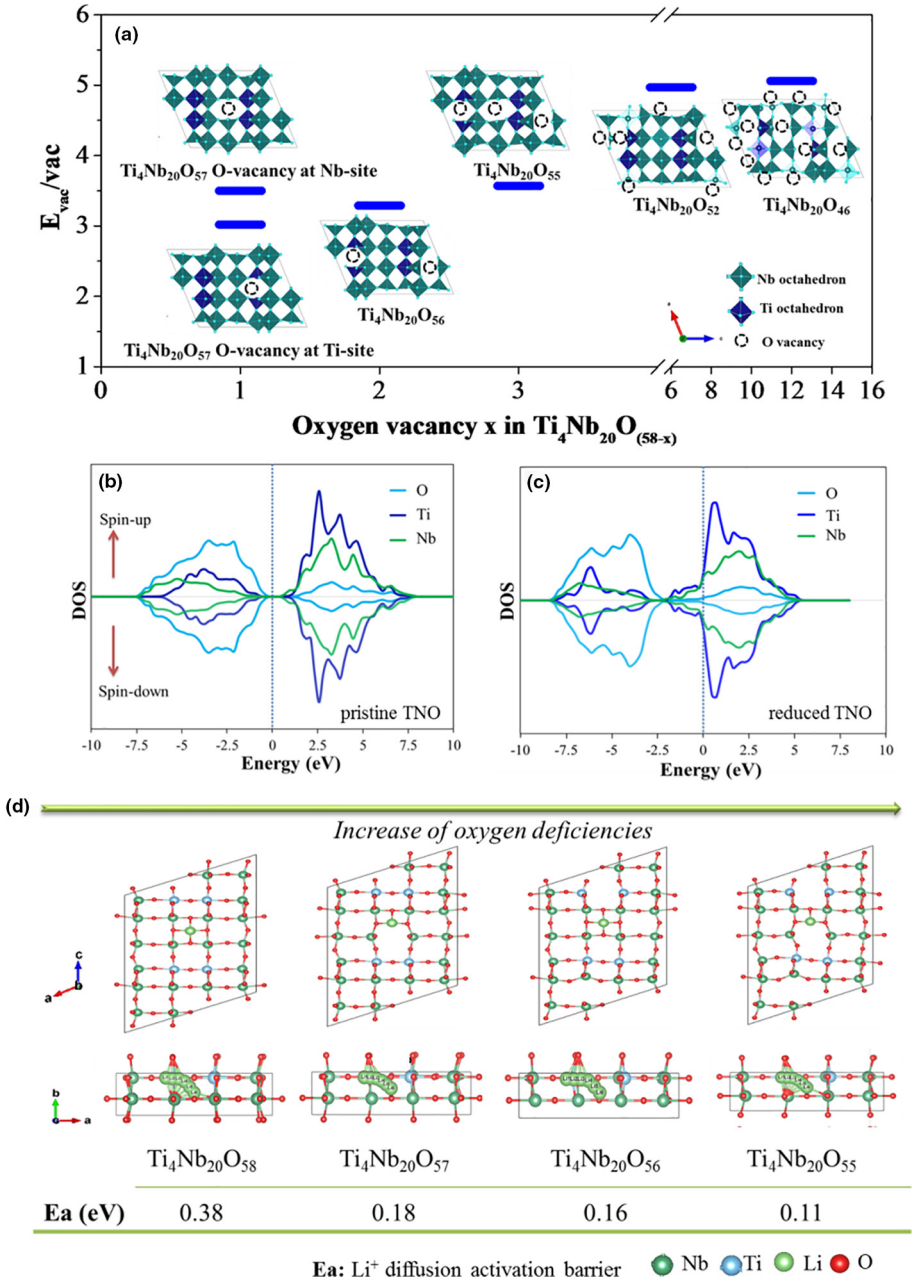

FIGURE 4

(a) The relationship of the formation energy of oxygen vacancy with its concentration and location in TNO structure; The calculated DOS of (b) pristine TNO ($Ti_4Nb_{20}O_{58}$) and (c) reduced TNO ($Ti_4Nb_{20}O_{55}$); (d) The Li-ion diffusion pathways and corresponding activation barrier for the pristine TNO and reduced TNO with increasing of oxygen deficiencies in the structures.

capacity was 334 mAh g^{-1} with an initial Coulombic efficiency of 90.1%. In contrast, when a pristine TNO (obtained from solid-state reaction) is used as the working electrode, the first discharge capacity was 272 mAh g^{-1} with an initial Coulombic efficiency of 89.7%. The stability both electrodes is shown to be sufficient in following cycles (Fig. S10). In our previous study, the lithiation capacity of carbonized PPy anode is about 110 mAh g^{-1} at 1 C rate in the potential range of 1–3 V [48]. However, considering the small carbon content in the composite (only ~1.8 wt.%), the contribution of the coated carbon layer to the sample capacity is assumed to be negligible. While it is still unclear as to the origin of the lower initial Coulombic efficiency, some speculate that a small amount of residual Li^+ stays in the structure after lithiation, resulting in a slight structure change [56]. The discharge capacity is larger than that typically reported for $Ti_xNb_yO_z$ compounds, such as $TiNb_{24}O_{62}$ (210–280 mAh g^{-1}) [4,5,57], $Ti_2Nb_{10}O_{29}$ (238–290 mAh g^{-1}) [6,20,58], and $TiNb_2O_7$ (213–251 mAh g^{-1}) [10,23,26,59]. The theoretical capacity of $Ti_2Nb_{10}O_{29}$ should be 396 mAh g^{-1} if a two-electron transfer per Nb atom ($Nb^{5+} \rightarrow Nb^{3+}$), and one-electron transfer per Ti atom ($Ti^{4+} \rightarrow Ti^{3+}$) is assumed. Therefore, the theoretical maximum amount of Li^+ per transition metal (Nb or Ti) should be 1.83 in the $Ti_2Nb_{10}O_{29}$ compound. In this work, the amounts of reversible inserted Li^+ per transition metal in the TNO@NC and pristine

Please cite this article in press as: T. Yuan et al., Materials Today (2021), https://doi.org/10.1016/j.mattod.2020.11.018

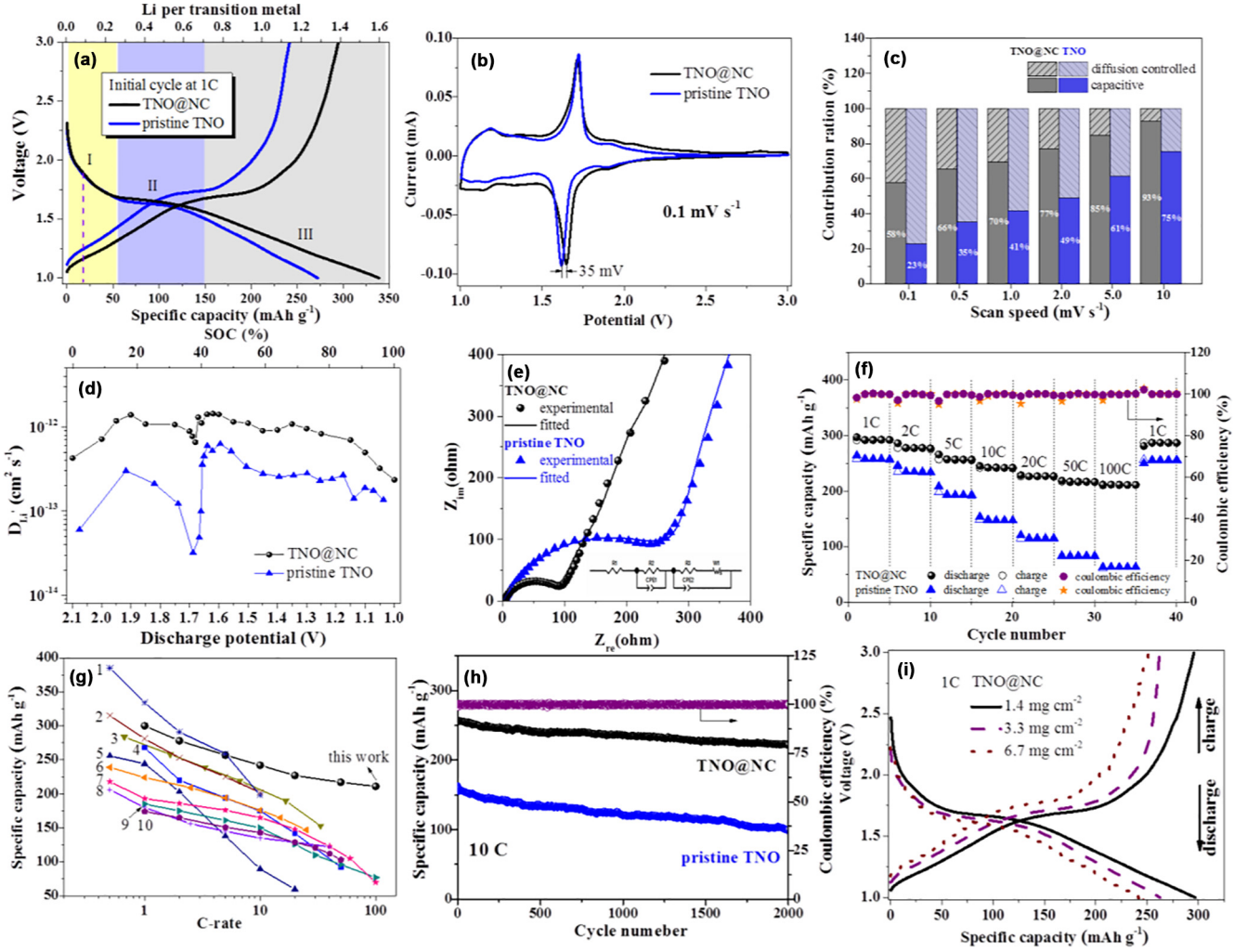

FIGURE 5

The electrochemical performance of the TNO@NC and pristine TNO electrodes for (a) Initial charge–discharge curves at 1 C rate and the corresponding Li^+ insertion per transition metal (Ti and Nb); (b) CV curves at the scanning rate of 0.1 mV s^{-1}; (c) Contribution ratio of capacitive and diffusion-controlled capacities at various scan rates; (d) D_{Li+} values were calculated from the GITT; (e) Complex impedance plots (scattered dots: experimental measurement; lines: fitted by equivalent circuit) (inset: the equivalent circuit); (f) Rate-cycle capacities at various current rates of 1–100 C; (g) Comparison of rate capabilities of TNO@NC with previously reported niobium- and titanium-based anode materials (1-$FeNb_{11}O_{29}$ [72], 2-$MoNb_{12}O_{33}$ [73], 3-$TiNb_{24}O_{62}$ [4], 4-$Ti_2Nb_{10}O_{29}$ [6], 5-$TiNb_2O_7$ [23], 6-TiO_2 [74], 7-$Nb_{18}W_{16}O_{93}$ [31], 8-Li_2O-TiO_2-H_2O [75], 9-T-Nb_2O_5 [76], 10-$Li_4Ti_5O_{12}$ [77]); (h) Long-term cycling at 10 C rate; (i) Charge–discharge curves of the TNO@NC electrode at 1 C with different mass loading.

TNO electrodes at a 1 C rate is 1.39 and 1.13 respectively. This indicates that the TNO@NC composite can insert more Li^+ than the pristine TNO at the same discharge rate. Furthermore, the discharge curves can be divided into three regions in Fig. 5a. *Region I* (located at 3–1.7 V) is considered as an initial intercalation process of Li^+. It is noteworthy that the slope of discharge curve of the TNO@NC anode is gentler than that of pristine TNO sample at ~1.9 V in *Region I*. The electrochemical reduction process reflected by this small plateau is still not fully described. Although it is generally believed that this small discharge plateau around 1.9 V can be ascribed to the reduction of $Ti^{4+} \rightarrow Ti^{3+}$ [7]. This conclusion is likely not correct because H-Nb_2O_5 also possesses the same charge/discharge plateau at ~1.9 V [11]. Guo et al. [25] verified that the charge/discharge plateau should correspond to the average redox potential of both Ti and Nb using X-ray absorption near edge spectroscopy. *Region II* (located at 1.6–1.7 V) exhibit a plateau in the middle of the discharge curves, which corresponds likely to a two-phase coexistence reaction process [20]. In this process, the Li-ions diffuse in the crystal lattice of TNO to keep the lowest energy, and the density of Li^+ in the crystal lattice increases accordingly [60]. The same situation occurs in the last solid-solution process shown in *Region III*. The increase in Li per transition metal for TNO@NC compared to the pure TNO material in *Region II* and *III* infers that the Li^+ diffusion rate in the TNO@NC composite is faster than that of the pristine TNO sample. This is in accordance with the DFT calculation results and will be further explored using cyclic voltammetry (CV), galvanostatic intermittent titration technique (GITT) and electrochemical impedance spectroscopy (EIS) techniques.

The corresponding redox process was investigated by CV. The initial three CV curves for TNO@NC electrode are shown in Fig. S11. A pair of redox peaks located at 1.64 V (reduction peak) and 1.71 V (oxidation peak) correspond to the voltage plateaus

Please cite this article in press as: T. Yuan et al., Materials Today (2021), https://doi.org/10.1016/j.mattod.2020.11.018

in Fig. 5**a**, which are most likely attributed to the Nb^{5+}/Nb^{4+} redox couple [20]. The difference between the redox peaks is only 0.07 V. Compared to the CV curve of the pristine TNO sample shown in Fig. 5b, the potential of the reduction peak of TNO@NC is 35 mV higher than that of the pristine TNO anode, indicating a smaller polarization and better reversibility than the pure sample [61]. A larger rectangle area appeared below 1.6 V that corresponded to electrochemical features of capacitance, which is accompanied by further reduction of Nb^{4+} to Nb^{3+} [7]. Furthermore, compared with the pristine TNO material, the TNO@NC electrode exhibits a larger rectangular area (Fig. 5b), implying that a more capacitive intercalation reaction for TNO@NC than that for the pure sample [62,63]. This capacitive reaction is expected to increase the rate capacity of the TNO@NC anode.

To describe the charge storage kinetics of the TNO@NC and pristine TNO electrodes, we calculated the capacitance contribution of the total capacity according to the CV measurements under various scan rates (Fig. S12). As shown in Fig. 5c, both the TNO@NC and pristine TNO samples possess considerable double-layer capacitive behavior during the charge–discharge process. This is attributed to the typical Roth-Wadsley structure with ordered ReO_3-matrix in TNO [64], which can provide a tunnel structure for realizing pseudocapacitive behavior accompanied by a faradaic charge transfer process with no crystallographic phase changes [65]. Furthermore, the capacitive contribution of TNO@NC electrode is much more than the pristine TNO electrode especially at high current rates, which should be due to the nanocrystalline structure of the TNO@NC inducing more contact interfaces between electrodes and electrolytes, and shortening the diffusion distance of Li^+ in the bulk of the TNO [66].

To better elucidate their ionic conductivity, the GITT of TNO@NC and pristine TNO electrodes were compared in Fig. 5d. The discharge Li^+ diffusion coefficient (D_{Li+}) values of the TNO@NC and pristine TNO anodes at different potentials are calculated based on the GITT potential responses in Fig. S13. The D_{Li+} increases during the initial Li^+ insertion process (corresponding to *Region I* in Fig. 5a) continuously until the first peak at 1.9 V, which indicates that Li^+ has better diffusion ability in the initial insertion stage of TNO. Yu et al. demonstrated that the Li-ions firstly intercalate into the lattice along b-axis and random occupy the sites located at face center of the Nb(Ti)O cubic [5]. Griffith et al. proved that the lithium ionic diffusion is anisotropic with much lower activation barriers in the tunnels along the b-axis [67]. Then, as the discharge potential continues to drop to 1.7 V (corresponding to *Region II* in Fig. 5a), the D_{Li+} suddenly drops, indicating there is slow Li^+ diffusion rate during the phase transition reaction process with a higher energy barrier for Li^+ motion across blocks [67]. In the subsequent solid-solution process (corresponding to *Region III* in Fig. 5a), the D_{Li+} rises again, and then decreases slightly with the increase of Li^+ density in the TNO lattice. The D_{Li+} values range from 2.4×10^{-13} to 1.5×10^{-12} cm^2 s^{-1} for the TNO@NC anode, and are an order of magnitude higher than that of the pristine TNO sample (from 3.0×10^{-14} to 4.8×10^{-13} cm^2 s^{-1}), which should be attributed to the existence of oxygen vacancies in the lattice of TNO@NC. When comparing the Li^+ diffusion coefficients in the TNO materials to the D_{Li+} of traditional $Li_4Ti_5O_{12}$ (10^{-16}–10^{-13} cm^2 s^{-1}) [68] or TiO_2 (10^{-18}–10^{-13} cm^2 s^{-1}) [69,70] anodes that were measured using GITT, TNO is qualitatively more conductive.

EIS experiments for the TNO@NC and pristine TNO anodes were conducted to understand the difference in electrochemical performance by identification of the electrode kinetics. Fig. 5e shows the Nyquist plots for the TNO@NC and pristine TNO electrodes after activation on the open circuit voltage of 1.7 V, which share a common feature of a depressed semicircle in high-to-medium frequency followed by a linear tail in the low-frequency region. The high-frequency intercept at the *x* axis is the combined resistance of the electrolyte, separator, and electrodes (ohmic impedance). The size of the semicircle in the high-to-medium frequency range is an indication of a complex reaction process for charge-transfer resistance, and the inclined line in the lower frequency region represents the Warburg impedance related to lithium diffusion through the TNO@NC and pristine TNO electrodes [71]. As shown in Fig. 5e, the ohmic impedances of both electrodes are almost the same, while the charge-transfer impedances are quite different. The much smaller charge-transfer resistant for TNO@NC is another evidence for the rapid electron and Li-ion transport, and thus expects to improve a high rate performance. This is also in good agreement with calculation results.

The rate behavior of the TNO@NC electrode with the mass loading of 1.4 mg cm^{-2} is shown in Fig. 5f. Compared to the pristine TNO sample and other samples calcined at 600, 700, 900 and 1000 °C (Fig. S14), the rate performance of the TNO@NC sample obtained at 800 °C is notable, which is attributed to the 800 °C calcined sample possesses both advantages of good crystallinity and smaller particle size. The reversible discharge capacities of TNO@NC electrode are 300, 278, 257, 242, 227, 217 and 211 mAh g^{-1} at 1, 2, 5, 10, 20, 50 and 100 C, respectively. At 100 C (only a 36 s charge/discharge duration time), 70.3% of the reversible capacity of the 1 C capacity is preserved, which is higher than that of the pristine TNO sample (24.4% capacity retention of 1 C). When the current rate returned to 1 C after 35 cycles, the TNO@NC electrode still exhibits a reversible capacity of 287 mAh g^{-1} (~96% capacity retention). Compared to other compounds in the $Ti_xNb_yO_z$, $M_xNb_yO_z$ or Ti-based family, the electrochemical performance of TNO@NC is notably better, especially at high cycling rates (Fig. 5g, Table S7) [4–6,10,23,31,55,72–81]. Fig. 5h shows the long-term stability of TNO@NC compared to TNO, maintaining a capacity of 223 mAh g^{-1} after 2000 cycles at 10 C with ~100% Coulomb efficiencies.

The rapid electron and Li-ion transport of the TNO@NC composite enables high capacity retention at practical mass loading. As shown in Fig. 5i, three different levels of mass loading from 1.4 to 6.7 mg cm^{-2} were investigated. The mass loading of 1.4 mg cm^{-2} correspond to typical loading amount for research studies, and the high mass loading of 6.7 mg cm^{-2} is representative of possible practical level. At 6.7 mg cm^{-2}, a reversible capacity of 248.5 mAh g^{-1} is reached at 1 C with very low overpotential. Even at a high rate of 10 C, a capacity of 176 mAh g^{-1} is maintained with 6.7 mg cm^{-2} loading, a decrease of only 26% from that of the 1.4 mg cm^{-2} electrode (Fig. S15). Fig. S16 shows the rate capability and cycle stability for a TNO@NC electrode with a mass loading of 6.7 mg cm^{-2}. Before the cycling sta-

Please cite this article in press as: T. Yuan et al., Materials Today (2021), https://doi.org/10.1016/j.mattod.2020.11.018

bility tests, the cell was first charged and discharged at 1 C for 5 cycles. The electrode shows suitable rate performance and cycling stability with a capacity retention of 92.0% after 500 cycles at 10 C.

To further evaluate the potential application of TNO@NC, the material was used in a full cell configuration to evaluate the volumetric and gravimetric energy and power density. To achieve a suitable energy density, we chose a commercial spinel $LiNi_{0.5}Mn_{1.5}O_4$ (LNMO) cathode, with an operating voltage of 4.7 V [82] to assemble a LNMO||TNO@NC full cell with an approximately 3 V working potential (Fig. 6a). The mass ratio of cathode active material to anode active material was balanced based on the practical capacities of LNMO (Fig. S17) and TNO@NC (Fig. 5a). The charge/discharge potential window of the LNMO||TNO@NC full cell is set to 0.5–4 V, which is calculated based on the differences of the corresponding charge/discharge cut-off potentials of the LNMO cathode and TNO@NC anode in Fig. 6a. Although this potential range is a little wider than that of the other reported LNMO||TNO full cells [83,84], the current study found no notable capacity degradation, as seen in Fig. 6b. The initial irreversible capacity loss (~15%) in the first charge process and low Coulombic efficiency in the second cycle (~95%) can be attributed to the formation of a cathode-electrolyte interface (CEI) film on the surface of the LNMO cathode and a structure change upon lithiation of TNO (Fig. S17a) [84]. Due to the poor rate performance of the commercial LNMO cathode (Fig. S17b), it is difficult to match the LNMO cathode and TNO@NC anode with a certain mass ratio for various current rates. The performance of the cell was only measured at 1 C. As shown in Fig. 6b, the specific capacity reaches ~240 mAh g^{-1} at 1 C (calculated based on the mass of the anodic active material). The long-term cycle performance of the LNMO||TNO@NC full cell is shown in Fig. 6c, which retains 80% capacity (186 mAh g^{-1}) after 300 cycles. Such cyclability is inferior to that of

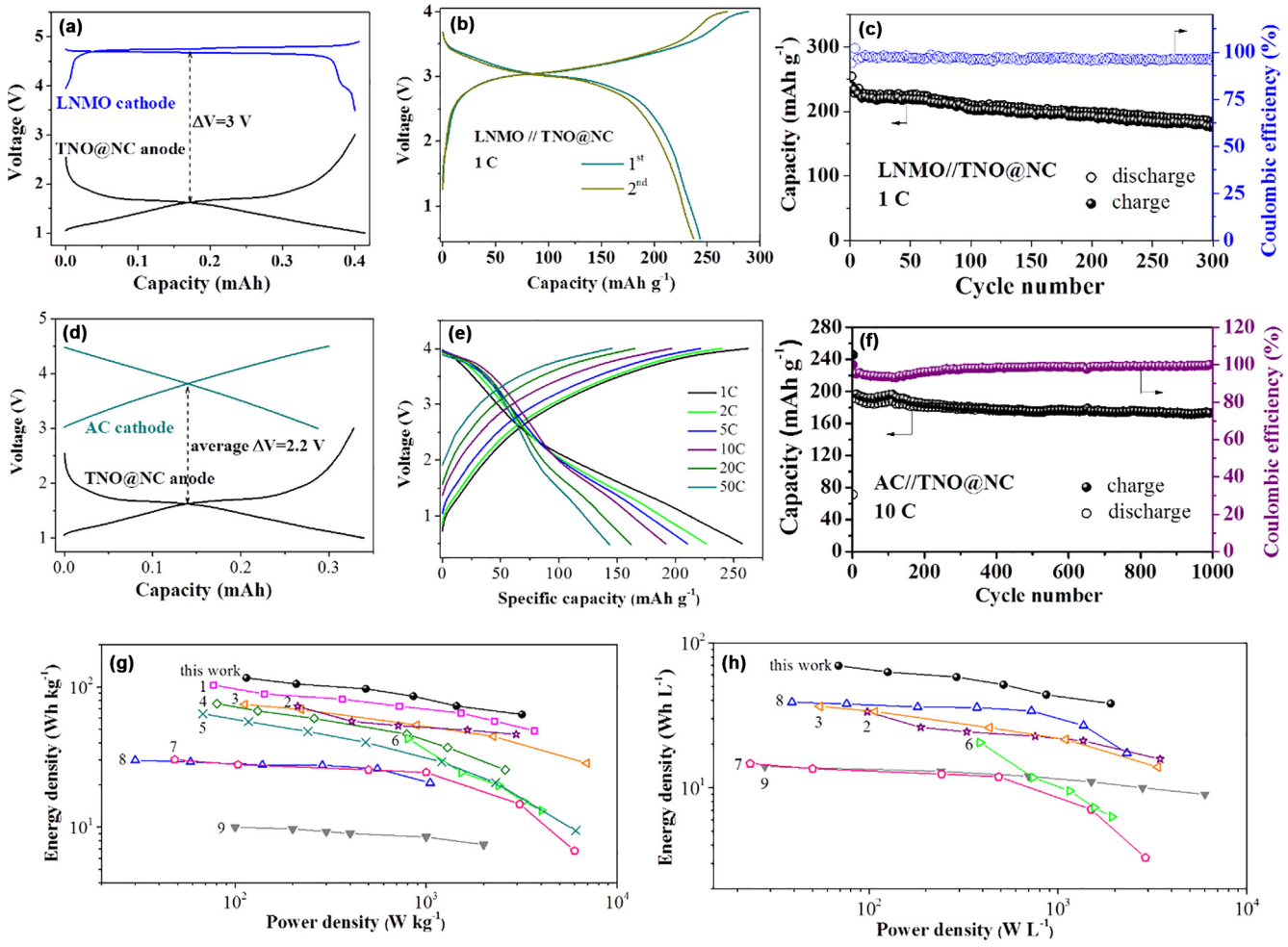

FIGURE 6

The electrochemical performance of: (a) Charge-discharge curves of the LNMO||Li (blue curves) and TNO@NC||Li (red curves) half-cell at 1 C rate; (b) Initial three charge–discharge galvanostatic curves of LNMO||TNO@NC full cell at 1 C rate with the cutoff voltages of 0.5–4 V; (c) Cycling performance for the LNMO||TNO@NC full cell at 1 C rate; (d) Charge–discharge curves of the AC||Li (dark cyan curves) and TNO@NC||Li (red curves) half-cell at 1 C rate; (e) Charge–discharge curves of the AC||TNO@NC hybrid LIC at various rates between 1 C and 50 C with the cutoff voltages of 0.5–4 V; (f) Long term cycling performance for the AC||TNO@NC hybrid LIC at 10 C rate; and Ragone plots of (g) gravimetric and (h) volumetric energy and power densities of the LNMO||TNO@NC lithium-ion full cell and AC||TNO@NC hybrid LIC in comparison with other various hybrid LIC/SIC systems (1-LIC: carbon nanosheet||HG-$TiNb_{24}O_{62}$ [4], 2-LIC: graphene||$TiNb_2O_7$ nanotube [85], 3-LIC: AC||m-Nb_2O_5-C [86], 4-SIC: MSP-20||Nb_2O_5@C/rGO [87], 5-LIC: MSP-20||T-Nb_2O_5@C [88], 6-LIC: AC||anatase-TiO_2 [89], 7-LIC: AC||Nb_2O_5-CNT [90], 8-LIC: AC||$Li_4Ti_5O_{12}$@graphene [91] 9-EDLC: AC||AC [91]).

Please cite this article in press as: T. Yuan et al., Materials Today (2021), https://doi.org/10.1016/j.mattod.2020.11.018

the TNO@NC half cell (Fig. 5h), which can attributed to the poor reversibility of the commercial LNMO cathode (Fig. S17c).

To fully utilized the high-rate performance of the TNO@NC anode, active carbon (AC) was used as a capacitive cathode to assemble hybrid LICs. Fig. 6d shows the charge/discharge profiles of AC cathode (with mass loading of 6.6 mg cm^{-2}) and TNO@NC anode (with mass loading of 1.0 mg cm^{-2}), with an average operating voltage of 2.2 V. The mass ratio was chosen according to the practical capacities of AC (Fig. S18) and TNO@NC. The corresponding charge/discharge curves of the AC||TNO@NC LIC at various rates are shown in Fig. 6e. When tested at 1, 2, 5, 10, 20 and 50 C, the AC||TNO@NC LIC delivers high reversible charge capacities of 257, 239, 221, 196, 165 and 145 mAh g^{-1}, respectively (calculated on the mass of the anodic active material). These rate capacities are lower than that of TNO@NC||Li half battery, possibly due to the increased electrode polarization of AC cathode (Fig. S18a). Fig. 6f shows a stable cycle stability of the AC||TNO@NC LIC over 1000 cycles at 10 C. After 1000 cycles, a capacity of 173 mAh g^{-1} is maintained with ~9.8% decrease.

In order to further evaluate the practical applicability of the LNMO||TNO@NC full battery and AC||TNO@NC LIC systems, a Ragone plot was constructed from the galvanostatic capacitance data based on the equation S6 and S7 in the *Supplementary Information* [66]. The gravimetric energy and power densities of the full battery system were calculated based on the total mass of cathode and anode active materials. For the LNMO||TNO@NC full battery system, the gravimetric energy density is 226 Wh kg^{-1} at a rate of 1 C. For the AC||TNO@NC hybrid LIC system, the gravimetric energy density is 116.1 Wh kg^{-1} at a power density of 114.6 W kg^{-1}; when the gravimetric power output reaches 3171.9 W kg^{-1}, the gravimetric energy density is 63.6 Wh kg^{-1} (Fig. 6**g**). When compared to other LIC systems the performance of the AC||TNO@NC LIC is notable, especially regarding volumetric energy and power densities Fig. 6h [4,85–91]. The volumetric energy density was calculated based on the tap densities of the active materials of anode (1.47 g cm^{-3} for TNO@NC) and cathode (2.0 g cm^{-3} for LNMO and 0.7 g cm^{-3} for AC) using the equation S8 and S9 in the *Supplementary Information*.

Conclusions

In summary, a high volumetric-power density TNO@NC composite anode was synthesized using a novel PPy-CVD method combined with thermal treatment. The enhanced electronic and ionic conductivity of the TNO@NC composite electrode with high tap density is attributed to the synergistic effect of the N-rich carbon coating, TiN-doping, formation of oxygen vacancies, and the micro-nano hierarchical architecture of the electrode, as confirmed by experimental measurements and DFT-based calculations. The behavior of the TNO@NC electrode in both LIB and LIC was characterized using several electrochemical techniques. In a half cell configuration, TNO@NC exhibited a reversible capacity of 300 mAh g^{-1} at 1 C rate and a superior rate performance of 211 mAh g^{-1} at 100 C with high stability. Additionally, the TNO@NC composite electrode retained high specific capacity as the mass loading was varied from 1.4 to 6.7 mg cm^{-2}. In a full cell configuration, a LNMO||TNO@NC LIB achieves a specific energy as high as 226 Wh kg^{-1}. Similarly, an AC||TNO@NC based hybrid LIC exhibits energy and power densities as high as 116.1 Wh kg^{-1} and 3171.9 W kg^{-1}, respectively, which represent a notable improvement over other similar LIC systems.

CRediT authorship contribution statement

Tao Yuan: Investigation, Data curation, Writing - original draft. **Sainan Luo:** Investigation, Data curation, Resources. **Luke Soule:** . **Jeng-Han Wang:** Software. **Yachen Wang:** . **Dewang Sun:** Investigation, Software. **Bote Zhao:** Resources, Methodology. **Wenwu Li:** Resources, Methodology. **Junhe Yang:** Resources, Formal analysis. **Shiyou Zheng:** Supervision, Conceptualization, Visualization. **Meilin Liu:** Supervision, Conceptualization, Visualization.

Declaration of Competing Interest

The authors declare that they have no known competing financial interests or personal relationships that could have appeared to influence the work reported in this paper.

Acknowledgements

We acknowledge the support of the National Science Foundation of China (51971146, 51671135, 21701030). We also acknowledge the support of the Program of Shanghai Subject Chief Scientist (17XD1403000), Shanghai Outstanding Academic Leaders Plan, the Innovation Program of Shanghai Municipal Education Commission (2019-01-07-00-07-E00015), CBMM, and the US National Science Foundation under award number DMR-1742828.

Appendix A. Supplementary data

Supplementary data to this article can be found online at https://doi.org/10.1016/j.mattod.2020.11.018.

References

[1] Y. Liu, Y. Zhu, Y. Cui, Nat. Energy 4 (2019) 540–550, https://doi.org/10.1038/s41560-019-0405-3.
[2] C. Choi et al., Nat. Rev. Mater. 5 (2020) 5–19, https://doi.org/10.1038/s41578-019-0142-z.
[3] J. Ding et al., Energy Environ. Sci. 8 (2015) 941–955, https://doi.org/10.1039/C4EE02986K.
[4] S. Li et al., NPG Asia Mater. 10 (2018) 406–416, https://doi.org/10.1038/s41427-018-0042-5.
[5] H. Yu et al., Nano Energy 54 (2018) 227–237, https://doi.org/10.1016/j.nanoen.2018.10.025.
[6] S. Lou et al., Energy Storage Mater. 11 (2018) 57–66, https://doi.org/10.1016/j.ensm.2017.09.012.
[7] S. Deng et al., Nano Energy 58 (2019) 355–364, https://doi.org/10.1016/j.nanoen.2019.01.051.
[8] L. Xing et al., J. Mater. Chem. A 7 (2019) 5760–5768, https://doi.org/10.1039/C8TA12497C.
[9] H. Park et al., Adv. Energy Mater. 5 (2015) 1401945, https://doi.org/10.1002/aenm.201401945.
[10] S. Lou et al., Nano Energy 34 (2017) 15–25, https://doi.org/10.1016/j.nanoen.2017.01.058.
[11] K.J. Griffith et al., J. Am. Chem. Soc. 138 (2016) 8888–8899, https://doi.org/10.1021/jacs.6b04345.
[12] R.S. Roth, A.D. Wadsley, Acta Crystallogr. 18 (1965) 724–730, https://doi.org/10.1107/S0365110X65001664.
[13] R.B.V. Dreele, K. Cheetham Anthony, S. Anderson John, P. R. Soc. London, A Math. Phys. Sci. 338 (1974) 311–326, https://doi.org/10.1098/rspa.1974.0088.
[14] K.J. Griffith, A. Senyshyn, C.P. Grey, Inorg. Chem. 56 (2017) 4002–4010, https://doi.org/10.1021/acs.inorgchem.6b03154.

Please cite this article in press as: T. Yuan et al., Materials Today (2021), https://doi.org/10.1016/j.mattod.2020.11.018

[15] D. Saritha, U.V. Varadaraju, Mater. Res. Bull. 48 (2013) 2702–2706, https://doi.org/10.1016/j.materresbull.2013.03.033.
[16] T. Yuan et al., Adv. Energy Mater. 7 (2017) 1601625, https://doi.org/10.1002/aenm.201601625.
[17] N. Delaporte et al., Mater. Adv. 1 (2020) 854–872, https://doi.org/10.1039/D0MA00227E.
[18] L. Yu, H.B. Wu, X.W.D. Lou, Adv. Mater. 25 (2013) 2296–2300, https://doi.org/10.1002/adma.201204912.
[19] T. Yuan et al., Energy Fuels (2020), https://doi.org/10.1021/acs.energyfuels.0c02732.
[20] X. Wu et al., Electrochem. Commun. 25 (2012) 39–42, https://doi.org/10.1016/j.elecom.2012.09.015.
[21] V. Aravindan et al., ChemSusChem 7 (2014) 1858–1863, https://doi.org/10.1002/cssc.201400157.
[22] S. Deng et al., Energy Storage Mater. 12 (2018) 137–144, https://doi.org/10.1016/j.ensm.2017.11.018.
[23] K. Tang et al., Adv. Energy Mater. 3 (2013) 49–53, https://doi.org/10.1002/aenm.201200396.
[24] X. Wang, G. Shen, Nano Energy 15 (2015) 104–115, https://doi.org/10.1016/j.nanoen.2015.04.011.
[25] B. Guo et al., Energy Environ. Sci. 7 (2014) 2220–2226, https://doi.org/10.1039/C4EE00508B.
[26] L. Fei et al., Nanoscale 5 (2013) 11102–11107, https://doi.org/10.1039/C3NR03594H.
[27] J. Han et al., ACS Energy Lett. 5 (2020) 1986–1995, https://doi.org/10.1021/acsenergylett.0c00851.
[28] K. Saravanan, K. Ananthanarayanan, P. Balaya, Energy Environ. Sci. 3 (2010) 939–948, https://doi.org/10.1039/C003630G.
[29] J. Ma et al., Nat. Commun. 10 (2019) 475, https://doi.org/10.1038/s41467-018-08233-3.
[30] Y. Huang et al., Angew. Chem. Int. Ed. 132 (2020) 20086–20090, https://doi.org/10.1002/ange.202008987.
[31] K.J. Griffith et al., Nature 559 (2018) 556–563, https://doi.org/10.1038/s41586-018-0347-0.
[32] M.R. Palacin, P. Simon, J.M. Tarascon, Acta Chim. Slov. 63 (2016) 7, https://doi.org/10.17344/acsi.2016.2314.
[33] Q. Cheng et al., J. Mater. Chem. A 2 (2014) 17258–17262, https://doi.org/10.1039/C4TA04184D.
[34] X. Xia et al., J. Mater. Chem. A 5 (2017) 21134–21139, https://doi.org/10.1039/C7TA07229E.
[35] A. Mohammadi et al., Synth. Met. 14 (1986) 189–197, https://doi.org/10.1016/0379-6779(86)90183-9.
[36] G. Kresse, J. Furthmüller, Phys. Rev. B: Condens. Matter Mater. Phys. 54 (1996) 11169–11186, https://doi.org/10.1103/PhysRevB.54.11169.
[37] G. Kresse, J. Hafner, Phys. Rev. B: Condens. Matter Mater. Phys. 47 (1993) 558–561, https://doi.org/10.1103/PhysRevB.47.558.
[38] G. Kresse, J. Hafner, Phys. Rev. B: Condens. Matter Mater. Phys. 49 (1994) 14251–14269, https://doi.org/10.1103/PhysRevB.49.14251.
[39] H. Cui et al., Sustainable Mater. Technol. 20 (2019), https://doi.org/10.1016/j.susmat.2019.e00094 e00094.
[40] D.M. Ceperley, B.J. Alder, Phys. Rev. Lett. 45 (1980) 566–569, https://doi.org/10.1103/PhysRevLett.45.566.
[41] J.P. Perdew, Y. Wang, Phys. Rev. B: Condens. Matter Mater. Phys. 45 (1992) 13244–13249, https://doi.org/10.1103/PhysRevB.45.13244.
[42] P.E. Blöchl, Phys. Rev. B: Condens. Matter Mater. Phys. 50 (1994) 17953–17979, https://doi.org/10.1103/PhysRevB.50.17953.
[43] G. Kresse, D. Joubert, Phys. Rev. B: Condens. Matter Mater. Phys. 59 (1999) 1758–1775, https://doi.org/10.1103/PhysRevB.59.1758.
[44] H.J. Monkhorst, J.D. Pack, Phys. Rev. B: Condens. Matter Mater. Phys. 13 (1976) 5188–5192, https://doi.org/10.1103/PhysRevB.13.5188.
[45] X. Zhang et al., Adv. Funct. Mater. 28 (2018) 1805618, https://doi.org/10.1002/adfm.201805618.
[46] A. Fahmi, C. Minot, Surf. Sci. 304 (1994) 343–359, https://doi.org/10.1016/0039-6028(94)91345-5.
[47] S. Luo et al., J. Mater. Chem. A 6 (2018) 15755–15761, https://doi.org/10.1039/C8TA05860A.
[48] T. Yuan et al., Chem. Commun. 52 (2016) 112–115, https://doi.org/10.1039/C5CC06964E.
[49] S. Deng et al., J. Power Sources 362 (2017) 250–257, https://doi.org/10.1016/j.jpowsour.2017.07.039.
[50] A.F. Orliukas et al., Solid State Ionics 271 (2015) 34–41, https://doi.org/10.1016/j.ssi.2014.09.037.
[51] K.S. Park et al., J. Am. Chem. Soc. 130 (2008) 14930–14931, https://doi.org/10.1021/ja806104n.
[52] T. Tian et al., Adv. Funct. Mater. (2020) 2007419, https://doi.org/10.1002/adfm.202007419.
[53] M.Z. Atashbar et al., Thin Solid Films 326 (1998) 238–244, https://doi.org/10.1016/S0040-6090(98)00534-3.
[54] Z. Xu et al., J. Mater. Sci. Technol. 28 (2012) 865–870, https://doi.org/10.1016/S1005-0302(12)60144-3.
[55] S. Deng et al., Nat. Commun. 11 (2020) 132, https://doi.org/10.1038/s41467-019-13945-1.
[56] C.P. Kocer et al., J. Am. Chem. Soc. 141 (2019) 15121–15134, https://doi.org/10.1021/jacs.9b06316.
[57] C. Yang et al., Nanoscale 8 (2016) 18792–18799, https://doi.org/10.1039/C6NR04992C.
[58] D. Pham-Cong et al., Electrochim. Acta 236 (2017) 451–459, https://doi.org/10.1016/j.electacta.2017.03.203.
[59] S. Li et al., J. Mater. Chem. A 4 (2016) 4242–4251, https://doi.org/10.1039/C5TA10510B.
[60] H. Yu et al., Nano Energy 38 (2017) 109–117, https://doi.org/10.1016/j.nanoen.2017.05.057.
[61] R.S. Nicholson, Anal. Chem. 37 (1965) 1351–1355.
[62] V. Augustyn, P. Simon, B. Dunn, Energy Environ. Sci. 7 (2014) 1597–1614, https://doi.org/10.1039/C3EE44164D.
[63] J. Wang et al., J. Power Sources 347 (2017) 259–269, https://doi.org/10.1016/j.jpowsour.2017.02.072.
[64] S. Iijima, J. Appl. Phys. 42 (1971) 5891, https://doi.org/10.1063/1.1660042.
[65] V. Augustyn et al., Nat. Mater. 12 (2013) 518–522, https://doi.org/10.1038/nmat3601.
[66] S. Luo et al., Adv. Funct. Mater. (2019) 1908309, https://doi.org/10.1002/adfm.201908309.
[67] K.J. Griffith et al., J. Am. Chem. Soc. 141 (2019) 16706–16725, https://doi.org/10.1021/jacs.9b06669.
[68] X. Hao, B.M. Bartlett, Adv. Energy Mater. 3 (2013) 753–761, https://doi.org/10.1002/aenm.201200964.
[69] J.-Y. Shin et al., Chem. Mater. 24 (2012) 543–551, https://doi.org/10.1021/cm2031009.
[70] C.W. Mason et al., RSC Adv. 3 (2013) 2935–2941, https://doi.org/10.1039/C2RA22847E.
[71] T. Yuan et al., Ceram. Int. 35 (2009) 1757–1768, https://doi.org/10.1016/j.ceramint.2008.10.010.
[72] D. Spada, I. Quinzeni, M. Bini, Electrochim. Acta 296 (2019) 938–944, https://doi.org/10.1016/j.electacta.2018.11.047.
[73] X. Zhu et al., J. Mater. Chem. A 7 (2019) 6522–6532, https://doi.org/10.1039/C9TA00309F.
[74] Y. Tang et al., Adv. Mater. 26 (2014) 6111–6118, https://doi.org/10.1002/adma.201402000.
[75] S. Wang et al., Nat. Commun. 8 (2017) 627, https://doi.org/10.1038/s41467-017-00574-9.
[76] H. Sun et al., Science 356 (2017) 599–604, https://doi.org/10.1126/science.aam5852.
[77] Z. Yao et al., Adv. Funct. Mater. 28 (2018) 1802756, https://doi.org/10.1002/adfm.201802756.
[78] Z. Yao et al., Energy Storage Mater. 25 (2020) 555–562, https://doi.org/10.1016/j.ensm.2019.09.027.
[79] K.J. Griffith et al., J. Am. Chem. Soc. 141 (2019) 16706–16725, https://doi.org/10.1021/jacs.9b06669.
[80] Y.-S. Lee, K.-S. Ryu, Sci. Rep. 7 (2017) 16617, https://doi.org/10.1038/s41598-017-16711-9.
[81] Y. Yuan et al., Chem. Eng. J. 374 (2019) 937–946, https://doi.org/10.1016/j.cej.2019.05.225.
[82] A. Manthiram, K. Chemelewski, E.-S. Lee, Energy Environ. Sci. 7 (2014) 1339–1350, https://doi.org/10.1039/C3EE42981D.
[83] G. Liang et al., Angew. Chem. Int. Ed. (2020), https://doi.org/10.1002/anie.202001454.
[84] J.T. Han, J.B. Goodenough, Chem. Mater. 23 (2011) 3404–3407, https://doi.org/10.1021/cm201515g.
[85] H. Li et al., J. Mater. Chem. A 3 (2015) 16785–16790, https://doi.org/10.1039/C5TA02929E.
[86] E. Lim et al., ACS Nano 8 (2014) 8968–8978, https://doi.org/10.1021/nn501972w.
[87] E. Lim et al., Adv. Funct. Mater. 26 (2016) 3711–3719, https://doi.org/10.1002/adfm.201505548.

Please cite this article in press as: T. Yuan et al., Materials Today (2021), https://doi.org/10.1016/j.mattod.2020.11.018

[88] E. Lim et al., ACS Nano 9 (2015) 7497–7505, https://doi.org/10.1021/acsnano.5b02601.
[89] H. Kim et al., Adv. Energy Mater. 3 (2013) 1500–1506, https://doi.org/10.1002/aenm.201300467.
[90] X. Wang et al., Adv. Energy Mater. 1 (2011) 1089–1093, https://doi.org/10.1002/aenm.201100332.
[91] T. Yuan et al., Ind. Eng. Chem. Res. 53 (2014) 10849–10857, https://doi.org/10.1021/ie501287a.

Please cite this article in press as: T. Yuan et al., Materials Today (2021), https://doi.org/10.1016/j.mattod.2020.11.018